

# Distributionally Robust Acceleration Control Barrier Filter for Efficient UAV Obstacle Avoidance

Dnyandeep Mandaokar<sup>1</sup> and Bernhard Rinner<sup>1</sup>

**Abstract**—Dynamic obstacle avoidance (DOA) for unmanned aerial vehicles (UAVs) requires fast reaction under limited onboard resources. We introduce the distributionally robust acceleration control barrier function (DR-ACBF) as an efficient collision avoidance method maintaining safety regions. The method constructs a second-order control barrier function as linear half-space constraints on commanded acceleration. Latency, actuator limits, and obstacle accelerations are handled through an effective clearance that considers dynamics and delay. Uncertainty is mitigated using Cantelli tightening with per-obstacle risk. A DR-conditional value at risk (DR-CVaR)-based early trigger expands margins near violations to improve DOA. Real-time execution is ensured via constant-time Gauss-Southwell projections. Simulation studies achieve similar avoidance performance at substantially lower computational effort than state-of-the-art baseline approaches. Experiments with Crazyflie drones demonstrate the feasibility of our approach.

## I. INTRODUCTION

Unmanned aerial vehicles (UAVs) are increasingly deployed in day-to-day services that require rapid responses to dynamic obstacles. Applications include urban UAV logistics, disaster response, and inspection in cluttered environments where obstacles such as other drones, birds, or humans may appear or move unpredictably [1]. To operate safely in these cases, UAVs must react fast to avoid collisions while maintaining stability. Dynamic obstacle avoidance (DOA) relies on high-rate perception and control and must handle perception uncertainty, latency, and limited computation under tight real-time constraints. Even a small perception-to-actuation latency can cause severe safety violations at high speeds [2]. In addition, vision and radio detection and ranging (RADAR) sensors produce high-rate measurements that further strain the capabilities of current DOA systems [3], [2].

Classical UAV sense-and-avoid approaches rely on trajectory optimization [4], [5], [6], nonlinear model predictive control (NMPC) [7], or reactive planners [8], [9]. While these methods can handle static or slowly moving obstacles, they are computationally demanding or rely on conservative safety margins, making them unsuitable for agile flights. Moreover, these optimization-based approaches often lack formal safety guarantees in the presence of fast and uncertain obstacle motion. Recently, control barrier functions (CBFs) emerged as a reliable framework to guarantee safety by ensuring forward invariance of a safe set [10], [11], [12] throughout the entire mission. The classical CBF is implemented using

a quadratic program (CBF-QP) and has been applied to ground robots, manipulators, and UAVs to enforce collision avoidance in real-time. Similarly, the existence of higher-order CBF (HOCBF) extends classical CBFs to handle higher relative-degree systems [10], which is crucial for UAVs with second-order dynamics. The implemented velocity-based formulations, such as VOCBF [13], encode safety in velocity space. Moreover, the CBF is integrated with differentiable optimization-based methods to enable smoother control pipelines [14]. Similarly, a probabilistic enumeration is introduced for stochastic risk allocation [15]. Runtime adaptive safety filtering and robust formulations have further broadened the applicability of CBFs in robotics [16], [17].

Despite this progress, the current CBF implementation faces limitations for DOA in UAVs. Existing CBF formulations act at the position or velocity level [13], [18], but do not provide closed-form acceleration-space constraints compatible with fast low-level thrust control. Although HOCBF implies extension of classical CBF to higher-order systems, it does not target acceleration or thrust as a control variable for DOA in UAVs. The HOCBF ensures safety at higher relative degrees [10], but requires solving QPs online, which is unsuitable for embedded flight controllers. Current implementations of CBF insufficiently address latency and uncertainty for DOA in UAVs. The ISSf-CBF [19] and tube-based formulations [20] consider robustness to input delay, but they are conservative and rely on iterative solvers. Probabilistic CBFs improve risk handling, but have not been adapted to acceleration-level constraints or integrated with hard real-time systems [15], [16]. Similarly, CBF with chance-constraints shows the importance of probabilistic risk margins for UAVs but remains velocity-centric [21]. The QP-based CBF solvers and sampling-based planners are too slow for high-rate DOA control, particularly on resource-constrained UAV hardware [18], [17], [10]. There are lighter and computationally efficient extensions of MPC, such as TinyMPC, which has been tested on Crazyflie but is under scrutiny for its fast DOA in UAVs [22].

In this paper, we address the current CBF-QP limitation for DOA in UAVs with a *distributionally robust acceleration control barrier function (DR-ACBF)*. DR-ACBF directly restricts UAV acceleration commands through safe, linear, half-space constraints. The half-space constraints specify the safe side of the projection plane for the UAV's acceleration, ensuring that the UAV remains within this region. We demonstrate that enforcing a linear acceleration-space constraint derived from the second-order CBF dynamics satisfies the original CBF inequality over a short horizon

<sup>1</sup>Dnyandeep Mandaokar and Bernhard Rinner are with the Institute of Networked and Embedded Systems, University of Klagenfurt, 9020 Klagenfurt, Austria (dnyandeep.mandaokar@aau.at and bernhard.rinner@aau.at).

under bounded uncertainty and latency assumptions. Additionally, the perception-to-actuation latency and uncertainty are handled by incorporating clearance buffering [2] and probabilistic tightening based on Cantelli inequalities [23], similar in spirit to stochastic CBFs [15], [16] but specialized for acceleration space. Moreover, an early-warning layer based on distributionally robust conditional value at risk (DR-CVaR) [24], [25], [26] is integrated to anticipate and adjust safety margins before any violation becomes imminent. Instead of solving QPs, we implement a constant-time Gauss-Southwell projection [27], [28] to enforce constraints, enabling real-time onboard execution.

In contrast to existing CBF-driven collision avoidance frameworks, our DR-ACBF framework provides: (i) explicit acceleration-space tightening to stay safe, (ii) low computational cost via cyclic projection, and (iii) probabilistic and latency-aware safety margins. We derive a closed-form line-of-sight (LoS) acceleration half-space with horizon-matched gains and a fixed-time projection enforcement with Gauss-Southwell. To the best of our knowledge, no prior works present an acceleration-space CBF filter with latency and risk tightening for UAV obstacle avoidance. The DR-ACBF achieves real-time, reliable UAV obstacle avoidance via acceleration-level CBFs, DR-CVaR trigger, and constant-time projection, reducing command time by over 37% while maintaining high safety and success rates as evaluated in a simulation study. Experiments with Crazyflie drones demonstrate the feasibility of our approach.

## II. PROBLEM FORMULATION

### A. Problem Statement

We model the UAV dynamics by second-order differential equations for simpler control design. We consider an acceleration-controlled quadrotor UAV operating in an environment with  $N$  dynamic obstacles. The obstacles are detected and tracked with typical trackers (e.g., SAFE-IMM tracker [29]), which deliver state estimates of the obstacles. The input space consists of the position  $p_e \in \mathbb{R}^3$ , velocity  $v_e \in \mathbb{R}^3$ , and acceleration  $a_e \in \mathbb{R}^3$  of the UAV as well as the relative position, velocity, and acceleration of the obstacle. A nominal controller provides an acceleration command  $a_n \in \mathbb{R}^3$ , while the UAV is subject to perception-to-actuation latency  $\Delta \geq 0$  and bounded actuation, i.e., limits for acceleration  $a_{\max} > 0$ , jerk  $j_{\max} > 0$ , and speed  $v_{\max} > 0$ . The objective of DR-ACBF is to design a real-time safety filter that modifies  $a_n$  to a safe command  $a_e \in \mathbb{R}^3$  while enforcing probabilistic collision avoidance under a user-specified global risk budget  $\alpha_{\text{total}}$  (see Figure 1).

### B. Dynamics and Relative Kinematics

Similar to the UAV, each dynamic obstacle  $i \in \{1, \dots, N\}$  is modeled as

$$\dot{p}_i = v_i, \quad \dot{v}_i = a_i, \quad \|a_i(t)\| \leq \hat{a}_{\max,i}, \quad (1)$$

where  $p_i, v_i, a_i \in \mathbb{R}^3$  denote the position, velocity, and acceleration, and  $\hat{a}_{\max,i} > 0$  is a learned upper bound on

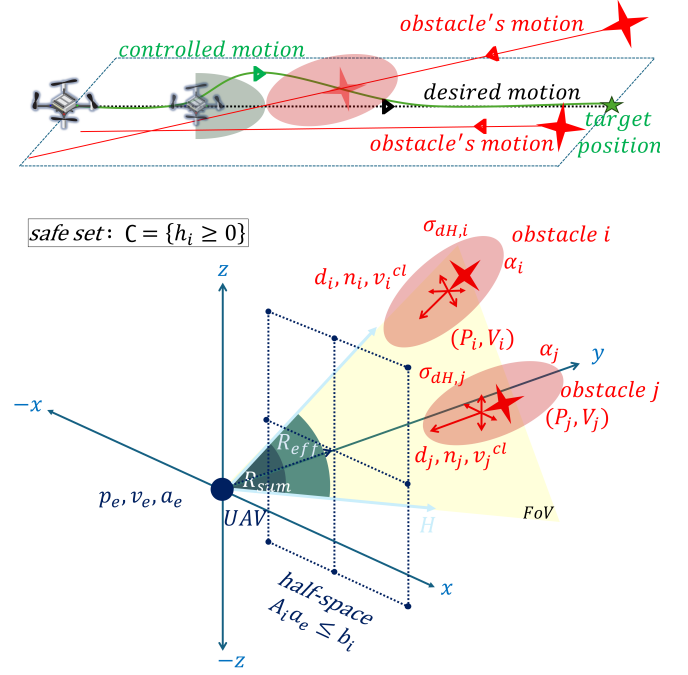


Fig. 1. Illustration of the proposed DR-ACBF framework. The UAV avoids dynamic obstacles (top) by constraining its acceleration within distributionally robust half-spaces marked in grey. The UAV view (bottom) depicts the projected half-space plane towards the obstacles. The effective clearance  $R_{\text{eff}}$  accounts for latency and actuation limits, while the obstacles' uncertainty ellipsoids  $\sigma_{dH,i}$  and risk levels  $\alpha_i$  tighten the constraints under sensing uncertainty. The safe set of action  $C$  ensures that the UAV's safe zone is not violated.

the obstacle acceleration. The relative position and velocity between the UAV and obstacle  $i$  are defined as

$$P_i = p_i - p_e, \quad V_i = v_i - v_e, \quad (2)$$

yielding the relative dynamics

$$\dot{P}_i = V_i, \quad \dot{V}_i = a_i - a_e. \quad (3)$$

From  $P_i$  and  $V_i$  we define the LoS quantities

$$n_i = \frac{P_i}{\|P_i\|}, \quad d_i = \|P_i\|, \quad v_i^{\text{cl}} = \max\{0, -n_i^\top V_i\}, \quad (4)$$

where  $n_i$  is the LoS unit vector,  $d_i$  is the range to the obstacle, and  $v_i^{\text{cl}}$  is the closing speed, capturing only approaching components of the relative velocity as illustrated in Figure 1.

### C. Tracking Uncertainty and Lookahead Prediction

The state and uncertainty estimates for each obstacle are provided by the tracker

$$\{\hat{p}_i, \hat{v}_i, \Sigma_i, \sigma_{v,i}\}_{i=1}^N, \quad (5)$$

where  $\Sigma_i \in \mathbb{R}^{3 \times 3}$  is the position covariance and  $\sigma_{v,i}$  is the standard deviation of the LoS component of the relative velocity uncertainty. The UAV position uncertainty is expressed by  $\Sigma_e$ . Given a lookahead horizon  $H > 0$ , the LoS distance prediction uncertainty is given as

$$\sigma_{dH,i} = \sqrt{n_i^\top (\Sigma_e + \Sigma_i) n_i + (H \sigma_{v,i})^2}. \quad (6)$$

#### D. Classical CBF Formulation

Ames et al. [12], [11] introduced the classical control Lyapunov functions (CLF)-CBF-QP architecture, which guarantees that an autonomous agent moves toward its goal while maintaining safety constraints. Let  $x \in \mathbb{R}^n$  denote the system state and  $u \in \mathbb{R}^m$  the control input. The control-affine dynamics are

$$\dot{x} = f(x) + g(x)u \quad (7)$$

where  $f(x)$  is the drift term and  $g(x)$  the control effectiveness matrix. A continuously differentiable function  $h : \mathbb{R}^n \rightarrow \mathbb{R}$  defines the safe set  $\mathcal{C}$ :

$$\mathcal{C} = \{x \in \mathbb{R}^n \mid h(x) \geq 0\}. \quad (8)$$

The Lie derivatives of  $h$  are  $L_f h(x) = \nabla h(x)^\top f(x)$  and  $L_g h(x) = \nabla h(x)^\top g(x)$ . The function  $h$  is a CBF with an extended class- $\mathcal{K}$  function  $\alpha(\cdot)$  such that

$$L_f h(x) + L_g h(x)u + \alpha(h(x)) \geq 0. \quad (9)$$

When (9) holds, the safe set  $\mathcal{C}$  is forward invariant. If  $x(0) \in \mathcal{C}$ , then  $x(t) \in \mathcal{C}$  for all  $t \geq 0$ . A continuously differentiable  $V : \mathbb{R}^n \rightarrow \mathbb{R}_{\geq 0}$  measures the distance to the desired goal state  $x_{\text{des}}$ . Therefore, the Lie derivatives are  $L_f V(x) = \nabla V(x)^\top f(x)$  and  $L_g V(x) = \nabla V(x)^\top g(x)$ .  $V$  is a CLF with a Lyapunov decay rate  $c > 0$  such that

$$\inf_u [L_f V(x) + L_g V(x)u + cV(x)] \leq 0. \quad (10)$$

This constraint ensures that some admissible  $u$  yields  $\dot{V}(x) \leq -cV(x)$  and thus stabilizes the system. At each control step, one computes  $u^*$  by solving the QP

$$\begin{aligned} (u^*, \delta^*) &= \arg \min_{u, \delta} \frac{1}{2} \|u - u_{\text{nom}}\|^2 + W\delta^2 \\ \text{s.t. } & L_f V(x) + L_g V(x)u + cV(x) \leq \delta, \\ & L_f h(x) + L_g h(x)u + \alpha(h(x)) \geq 0, \\ & \delta \geq 0. \end{aligned} \quad (11)$$

where  $u_{\text{nom}}$  is a nominal control,  $W$  is a weighting coefficient, and  $\delta$  relaxes the goal constraint. The CBF inequality (9) strictly enforces safety while the CLF (10) is a soft constraint, i.e., performance is relaxed when safety requires it, as in (11).

### III. METHOD

Figure 2 shows our system block diagram, where the contribution of this paper (DR-ACBF avoidance) is depicted in blue. This part combines obstacle acceleration estimation and risk association with DR-CVaR to provide an avoidance warning, which serves as input to the ACBF and Gauss-Southwell projection to provide the avoidance acceleration. DR-ACBF does not integrate a trajectory planner; instead, it utilizes the target position as the next lookahead.

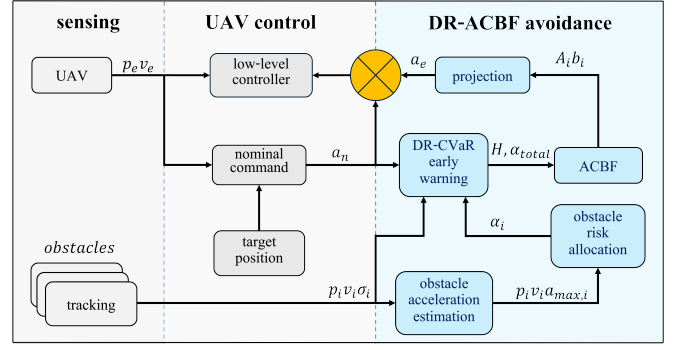


Fig. 2. System block diagram. The process begins with sensing the UAV and obstacle states. UAV control generates a nominal acceleration command  $a_n$ , which is corrected by DR-ACBF avoidance. The DR-CVaR layer provides an early warning, the acceleration estimation, and risk allocation to compute the safety constraints. Finally, ACBF and projection replace  $a_n$  with the safe acceleration command  $a_e$  to avoid obstacles.

#### A. Acceleration CBF

We model the UAV dynamics similar to Equations (3) with  $\|a_e\| \leq a_{\text{max}}$ :

$$\dot{p}_e = v_e, \quad \dot{v}_e = a_e. \quad (12)$$

The combined sum of obstacle and UAV radius is  $R_{\text{sum}} = R_{\text{uav}} + R_{\text{obs}}$  as illustrated in Figure 1. Then the barrier function for distance is

$$h_i(P_i) = \|P_i\|^2 - R_{\text{sum}}^2 \quad (13)$$

which satisfies  $h_i \geq 0$  in the safe region. Differentiating twice and substituting (12) gives

$$\dot{h}_i = 2P_i^\top V_i, \quad \ddot{h}_i = 2V_i^\top V_i + 2P_i^\top (a_i - a_e). \quad (14)$$

Therefore, safety is ensured when the second-order barrier condition holds

$$\ddot{h}_i + k_1 \dot{h}_i + k_2 h_i \geq 0, \quad k_1, k_2 > 0, \quad (15)$$

where  $k_1$  damps the approach velocity and  $k_2$  penalizes distance violation. In order to project the second-order condition into an acceleration half-space, we linearize it over a short lookahead horizon  $H > 0$  and eliminate the obstacle acceleration  $a_i$  by worst-case padding, yielding an affine constraint in the UAV acceleration

$$A_i a_e \leq b_i, \quad (16)$$

$$A_i = n_i^\top, \quad b_i = \frac{2}{H^2} \left( d_i - R_{\text{eff},i} - v_i^{\text{cl}} H \right) \quad (17)$$

where  $R_{\text{eff},i}$  is the effective clearance that accounts for sensing and actuation latencies. Each obstacle thus defines one linear half-space of safe accelerations. The effective clearance in distance is enlarged to account for perception latency, actuation limits, and jerk bound:

$$R_{\text{eff},i} = R_{\text{sum}} + v_{\text{max}} \Delta + \frac{1}{2} a_{\text{max}} \Delta^2 + \frac{1}{6} j_{\text{max}} H^3 + \frac{1}{2} \hat{a}_{\text{max},i} H^2 \quad (18)$$

where  $v_{\text{max}}$  is the UAV speed limit,  $a_{\text{max}}$  and  $j_{\text{max}}$  are acceleration and jerk bounds,  $\Delta$  is total perception-to-actuation

latency, and the  $\hat{a}_{\max,i}$  is the learned bound on obstacle acceleration. The sliding-mode differentiator (SMD) is used to compute the  $\hat{a}_{\max,i}$  with a user-defined  $a_{\max,i}$ , aiming to keep it large to address the worst possible acceleration of obstacles. This is explained in detail in the next sections.

In order to compensate for the system's latency changes, the latency contribution inside  $R_{\text{eff}}$  is bounded by  $v_{\max}\Delta + \frac{1}{2}a_{\max}\Delta^2$ . While the new command is held over  $H$  with bounded jerk  $j_{\max}$ , the worst additional shrink from the acceleration ramp is upper-bounded by  $\frac{1}{6}j_{\max}H^3$ . The obstacle displacement over  $H$  is limited by  $\frac{1}{2}\hat{a}_{\max,i}H^2$ . Summing up all these components to  $R_{\text{sum}}$  yields (18). The  $\Delta$  includes pre-actuation latency to account for delays in activating the controls. The impact of such latency on safe high-speed navigation with bounded acceleration is analyzed in [2]. The trackers provide estimates of position and velocity [29]. Therefore, if we consider the position and velocity covariance from the tracker, the LoS variance is bounded by Eq. (6).

Over a short lookahead horizon  $H$ , the coefficients  $k_1 = 2/H$  and  $k_2 = 2/H^2$  ensure that any acceleration satisfying the affine constraint maintains a non-decreasing barrier value of  $h_i(t)$  over  $H$ . These coefficients follow from the second-order Taylor expansion of  $h_i(t)$  over the horizon  $H$ . Enforcing the short-horizon condition  $h_i(t+H) \geq 0$  yields  $k_1$  and  $k_2$ .

### B. Obstacle Risk Allocation

Risk allocation helps to select the appropriate response in case of multiple obstacles. We allocate a global risk budget  $\alpha_{\text{total}} \in (0,1)$  among  $N$  obstacles indexed by  $i, j \in \{1, 2, \dots, N\}$ . We assign obstacle budgets  $\alpha_i$  using a proximity-velocity weighting with  $v_i^{\text{cl}}$  (4) for some small  $\varepsilon > 0$  to ensure numerical safety:

$$r_i = \frac{v_i^{\text{cl}}}{\max_j v_j^{\text{cl}} + \varepsilon}, \quad w_i = \frac{1 + r_i}{\max(d_i, 10^{-3})}, \quad (19)$$

$$\alpha_i = \frac{w_i}{\sum_j w_j} \alpha_{\text{total}}. \quad (20)$$

The  $10^{-3}$  term in  $w_i$  prevents division by zero. The per-obstacle budgets sum to the global risk,  $\sum_i \alpha_i = \alpha_{\text{total}}$ . The  $r_i$  is a normalized closing-speed score that prioritizes obstacles approaching faster than others, and  $w_i$  is the combined weight for approach urgency and proximity. Therefore, the provided obstacle budgets  $\alpha_i$  with a one-sided Cantelli inequality [23] yields the tightening factor  $\lambda_i$

$$\Pr(d_{\text{true},i}(t+H) \geq d_{\text{pred},i}(t+H) - \lambda_i \sigma_{dH,i}) \geq 1 - \alpha_i, \quad (21)$$

$$\lambda_i = \sqrt{\frac{1 - \alpha_i}{\alpha_i}}, \quad (22)$$

which allows to tighten the half-space right-hand. Substituting into (16) gives the tightened constraint:

$$A_i a_e \leq \frac{2}{H^2} \left( d_i - R_{\text{eff},i} - v_i^{\text{cl}} H - \lambda_i \sigma_{dH,i} \right). \quad (23)$$

Temporal safety over  $[t, t+H]$  is ensured by the clearance  $R_{\text{eff},i}$  (18) and the Cantelli tightening (21) (22). The clearance  $R_{\text{eff},i}$  expands the safety margin, while the tightening term  $\lambda_i \sigma_{dH,i}$  bounds stochastic errors, which yields a closed-form bound for the collision barrier (23). This tightened bound maintains the ACBF inequality (15) with probability of at least  $1 - \alpha_i$ . Consequently, the safe set  $C$  remains forward invariant under sensing uncertainty and latency.

### C. Obstacle Acceleration Estimation

In addition to risk allocation, DOA needs to estimate acceleration bounds for the obstacle to maintain a safe distance in all cases. In order to assess the unknown acceleration of an obstacle  $\hat{a}_{\max,i}$ , we assume piecewise constant relative acceleration over the lookahead  $H$  and compute the upper bound  $\hat{a}_{\max,i}$  via higher-order SMD [30], [31]. From measured obstacle velocity  $v_i$ , the SMD internal states  $(z_0, z_1, z_2)$  yield a robust estimate  $\hat{a}_i = z_1$  and (if required) an estimate  $\hat{j}_i = z_2$ . The differentiator dynamics are given as

$$\begin{aligned} \dot{z}_0 &= -l_1 |z_0 - v_i|^{1/2} \text{sgn}(z_0 - v_i) + z_1 \\ \dot{z}_1 &= -l_2 \text{sgn}(z_0 - v_i) \\ \dot{z}_2 &= -l_3 \text{sgn}(z_2 - \dot{z}_1) \end{aligned} \quad (24)$$

where  $(z_0, z_1, z_2)$  are internal states and  $l_1, l_2, l_3 > 0$  are design gains. The SMD output provides a robust, noise-insensitive estimate of the true derivative  $\dot{v}_i = a_i$  with finite-time convergence. The estimated acceleration bound is updated online as

$$\hat{a}_{\max,i} \leftarrow \max(\hat{a}_{\max,i}, \|\hat{a}_i\|) \quad (25)$$

which ensures a conservative envelope on obstacle acceleration used in the effective clearance (18) and allows the safety margin to expand automatically when obstacles exhibit more aggressive maneuvers.

### D. DR-CVaR Early Warning

Additionally, the framework uses an early trigger to complement ACBF based on conditional value at risk (CVaR) [24], [25]. We introduce a real-time distributionally robust CVaR (DR-CVaR) layer that operates in conjunction with the proposed ACBF controller. The DR-CVaR predicts the obstacle's future state to check if it violates a dynamic distance to the UAV. This layer does not enforce the barrier constraints directly; it only anticipates imminent violations and triggers avoidance early. Once triggered, the system hands control to the ACBF block, which operates on horizon  $H$ .

For each obstacle  $i$  and prediction time  $t_k \in [0, \tau]$ , the set of propagated sample states is defined by  $P^{(n)}(t_k)$  and  $V^{(n)}(t_k)$  for the  $n$ -th sample prediction. The  $\tau$  denotes the reaction latency and handles preemptive risk checks, while  $H$  ensures constraint satisfaction. For each sample  $P^{(n)}, V^{(n)}$ , we define the LoS unit vector, i.e.,  $n^{(n)}$  and the closing speed  $v^{(n)}$  computed as in Eq. (4). This helps to estimate a dynamic

distance for the  $n$ -th sample

$$D_{\text{dyn}}^{(n)} = v^{(n)}\tau + \frac{(v^{(n)})^2}{2(a_e + a_i)} \quad (26)$$

where  $a_i$  and  $a_e$  denote the available deceleration magnitudes of the obstacle and the UAV deceleration. Then, the safe distance is

$$D_{\text{safe}}^{(n)} = R_{\text{sum}} + D_{\text{dyn}}^{(n)}. \quad (27)$$

The corresponding violation term is

$$Z^{(n)} = D_{\text{safe}}^{(n)} - \|P^{(n)}(t_k)\|. \quad (28)$$

To guard against distributional mismatch, we add a Wasserstein upshift  $\epsilon L_Z$  with radius  $\epsilon$  and Lipschitz constant  $L_Z$  [26]. We adopt the standard empirical CVaR definition using the worst  $m$  samples [24], [25]

$$\text{CVaR}_{\beta}^{\text{DR}}(Z) = \frac{1}{m} \sum_{n \in \text{worst } m} Z^{(n)} + \epsilon L_Z \quad (29)$$

where  $m = \lceil \beta N_s \rceil$  with  $\beta \in (0, 1)$  specifies how much of the worst-case distribution we consider.  $N_s$  denotes the number of Monte-Carlo samples per obstacle used for short-horizon prediction. We set  $\epsilon$  as a robust radius tied to the sample spread. If  $\max_k \text{CVaR}_{\beta}^{\text{DR}}(Z) \geq 0$ , the early warning layer triggers avoidance before any barrier violation is imminent. It replaces the nominal acceleration  $a_n$  by an evasive avoid acceleration  $a_e$  with a projection from ACBF. It tightens the ACBF constraints and  $R_{\text{eff}}$  by reducing  $\alpha_{\text{total}}$  and increasing  $H$  for one cycle. The  $\beta$  controls the tail fraction for prediction-based early warning, and the  $\alpha_{\text{total}}$  provides the probabilistic tightening of the ACBF constraints.

#### E. Gauss-Southwell Projection

To further improve the real-time capabilities, we avoid QP and apply a deterministic Gauss-Southwell (most violated constraint) projection to a nominal acceleration command  $a_0 = a_n$  [28], [27]

$$i^* = \arg \max_i (A_i a_l - b_i) \quad (30)$$

where  $i^*$  is the index of the most violated constraint and  $a_l$  is the acceleration iterate at the current step of the projection loop. The projection is iterated for a fixed number of steps. At each iteration  $l$ , the acceleration is updated as

$$a_{l+1} = a_l - \omega \frac{(A_{i^*} a_l - b_{i^*})_+}{\|A_{i^*}\|^2} A_{i^*}^\top \quad (31)$$

$$a_{l+1} \leftarrow \Pi_{\|a\|_\infty \leq a_{\text{max}}}(a_{l+1})$$

where  $\omega \in (0, 1]$  is a relaxation coefficient in the projection algorithm, which is tuneable empirically for fastest convergence. The projection loop runs for a fixed iteration budget, which is typically limited to 15 iterations. The resulting  $a_e = a_l$  is the safe acceleration command. The iteration (31) is a relaxed Gauss-Southwell projection onto the most violated halfspace, followed by projection onto the acceleration space (16). This scheme is known to be numerically stable [28], [27] and iterates toward the feasible set  $C$  (8).

## IV. SIMULATION STUDY

In this section, we compare our DR-ACBF with three other collision avoidance methods in a simulation study. We use the classical CBF-QP [12], [10], robust policy CBF (RP-CBF) [16], and model predictive control (MPC) [7], [32], [22] as baselines and integrate the DR-CVaR early trigger for a fair comparison of the ACBF improvement.

We use the following metrics for our comparison: The success rate  $s$  is defined as the ratio of simulation runs that successfully avoid collisions over all runs. The computation time  $t_{\text{cp}}$  is the processing time of our avoidance algorithm (from acceleration estimation to projection in Figure 2). The command time  $t_{\text{cm}}$  represents the control latency, defined as the time from the trigger to issuing the first avoid command. The reaction time  $t_r$  represents the duration from the trigger to the first detectable avoid action and combines the command time with the dynamics of the UAV. The minimum separation  $d_s$  represents the minimum distance between the UAV and the obstacle during the avoidance maneuver. Finally,  $v_{\text{cl}}$  represents the speed of the obstacle towards the UAV.

#### A. Simulation Setup

We simulate the proposed method in MATLAB on a CPU-only laptop using the UAV Scenario Toolbox [33] at 100 Hz. The dynamic obstacles move across the LoS with random initial velocities with lower bound  $v_{\text{min}} = 5$  m/s. The obstacles move with their initial velocity along a straight-line trajectory. The trajectory of one obstacle diagonally intersects the path of the UAV, whereas the other obstacle directly moves towards the UAV. Both obstacles start at a distance of 150 m and 200 m from the UAV, respectively. The UAV and obstacle radius are  $R_{\text{uav}} = 0.15$  m and  $R_{\text{obs}} = 0.15$  m resulting in  $R_{\text{sum}} = 0.3$  m. The actuation limits are bounded with  $\|a_e\|_\infty \leq 6$  m/s<sup>2</sup>. A 3D RADAR sensor data generator [34] with 80 azimuth  $\times$  20 elevation, and range of 150 m is used to generate realistic mmWave RADAR data for the GNN-based SAFE-IMM obstacle tracker [29].

DR-ACBF uses a one-step global collision risk budget of  $\alpha_{\text{total}} = 0.10$ , distributed among obstacles according to proximity  $d_i$  and closing speed  $v_i^{\text{cl}}$ . A single horizon per cycle  $H$  is selected via coarse search  $H \in [H_{\text{min}}, H_{\text{max}}]$  with user given time horizon  $H_{\text{max}} = 0.4$  s and  $H_{\text{min}} = 0.15$ . The coarse search selects the largest feasible  $H$ , which maximizes clearance while still satisfying all constraints. Obstacle acceleration envelopes  $\hat{a}_{\text{max},i}$  are learned online using an SMD differentiator with  $(\gamma, L_0, L_1, L_2) = (1.5, 4, 3, 2)$ . Safe accelerations are obtained via a constant-time Gauss-Southwell projector with 12 base iterations and relaxation  $\omega = 1.0$ .

The complete DOA consists of the avoidance action, followed by a hover at the bypass position, and mission continuation towards the next target position. The UAV should hover with time to stop within  $t_s = 0.5$  s and braking intensity of  $k_s = 1.0$ . The lateral clearance  $d_{\text{cl}}$  is 0.05 m, and minimum hold time after avoid  $t_{\text{hd}}$  is 3 s. The DR-CVaR early-warning trigger runs before projection with  $\beta = 0.05$



and a reaction latency of  $\tau = 0.02$  s. In our experiments, we set the Wasserstein radius  $\epsilon$  to 0.05 for numerical stability.

### B. Simulation Results

Table I compares the proposed DR-ACBF approach against conventional CBF, MPC, and recent RP-CBF techniques with identical simulation scenarios of one or two dynamic obstacles. Our DR-ACBF outperforms the other techniques in all time measurements. Particularly, the processing time is reduced by 19% to 42%, which is important for embedded platforms. Despite the reduced computational effort, DR-ACBF maintains comparable performance with a mean success rate  $s$  of 84.85% and the minimum separation  $d_s$  of 1.844 m, satisfying safety constraints throughout the mission.

TABLE I  
COMPARISON OF DR-ACBF WITH THREE BASELINE DOA METHODS  
USING 3000 SIMULATIONS FOR EACH SCENARIO.

Method	Obstacle	$s$ (%)	$v_{cl}$ (m/s)	$t_r$ (ms)	$t_{cm}$ (ms)	$t_{cp}$ (ms)	$d_s$ (m)
MPC	1	86.0	7.13	16.00	6.00	-	0.909
	2	83.4	9.80	13.56	3.08	-	3.040
	Mean	<b>84.7</b>	<b>8.36</b>	<b>14.85</b>	<b>4.65</b>	<b>0.591</b>	<b>1.888</b>
CBF-QP	1	86.1	7.14	25.25	3.15	-	0.913
	2	83.6	9.82	12.95	2.31	-	3.098
	Mean	<b>84.9</b>	<b>8.36</b>	<b>19.62</b>	<b>2.77</b>	<b>0.461</b>	<b>1.914</b>
RP-CBF	1	86.0	7.13	15.35	2.68	-	0.908
	2	83.4	9.80	23.94	2.54	-	3.040
	Mean	<b>84.77</b>	<b>8.36</b>	<b>19.29</b>	<b>2.62</b>	<b>0.425</b>	<b>1.844</b>
DR-ACBF	1	86.1	7.14	12.29	1.68	-	0.913
	2	83.5	9.65	14.08	1.58	-	2.990
	Mean	<b>84.85</b>	<b>8.30</b>	<b>11.98</b>	<b>1.64</b>	<b>0.347</b>	<b>1.844</b>

### C. Sensitivity Analysis and Ablation

TABLE II  
SENSITIVITY ANALYSIS OF KEY DR-ACBF PARAMETERS AVERAGED  
FOR 1000 SIMULATION RUNS.

$H_{\max}$ (s)	$d_{cl}$ (m)	$t_{hd}$ (m)	$s$ (%)	$v_{cl}$ (m/s)	$t_r$ (ms)	$t_{cm}$ (ms)	$t_{cp}$ (ms)	$d_s$ (m)
0.4	3	0.2	82.5	8.18	12.74	2.24	0.475	1.881
0.2	3	0.2	79.8	8.16	11.88	1.58	0.312	1.822
0.8	3	0.2	82.5	8.28	12.35	1.85	0.382	2.105
0.4	1	0.2	82.3	8.02	12.87	2.07	0.234	1.864
0.4	4	0.2	77.6	7.16	12.16	1.66	0.423	2.054
0.4	3	0.1	82.6	7.10	11.92	1.72	0.362	1.924
0.4	3	0.4	82.6	8.18	12.17	1.97	0.403	1.945

To test the robustness of the proposed method, we conducted a sensitivity analysis using 1000 simulation runs and varying three key parameters. Table II summarizes the sensitivity of DR-ACBF to the key parameters maximum time horizon  $H_{\max}$ , clearance distance  $d_{cl}$ , and hold time  $t_{hd}$ . Each parameter was varied independently while keeping the others fixed. The key parameters of the first row in Table II correspond to the simulation results over 3000 runs (Table I). Results indicate that DR-ACBF maintains a consistent  $s$  above 77% and shows no significant change in  $t_r$  and  $d_s$

across all key parameter configurations. Minor variations in  $H_{\max}$  shows a reduction in  $t_{cm}$  and  $t_{cp}$ .

TABLE III  
ABLATION STUDY OF DR-CVaR TRIGGER IN ACBF FOR 1000 RUNS.

DR-CVaR	Obstacle	$s$ (%)	$v_{cl}$ (m/s)	$t_r$ (ms)	$t_{cm}$ (ms)	$d_s$ (m)
ON	1	80.0	9.48	12.11	2.11	2.969
	2	84.7	7.10	12.95	2.35	0.985
	Mean	<b>82.5</b>	<b>8.18</b>	<b>12.74</b>	<b>2.24</b>	<b>1.881</b>
OFF	1	32.00	9.70	11.74	1.74	0.707
	2	37.90	8.01	12.06	2.06	0.858
	Mean	<b>34.90</b>	<b>8.70</b>	<b>11.93</b>	<b>1.93</b>	<b>0.796</b>

Finally, we conduct an ablation study to evaluate the effectiveness of the proposed early trigger DR-CVaR in ACBF. In order to isolate the contribution of the proposed DR-CVaR trigger, we compared it with a baseline, i.e., a minimal trigger that uses a single-time Gaussian chance constraint at the time of closest approach (DR-CVaR OFF in Table III). All other components (geometry, dynamics, parameters) remain identical across 1000 runs. As shown in Table III, activating DR-CVaR leads to a substantial improvement in performance, increasing the success rate  $s$  from 34.9% to 82.5% while maintaining comparable response times. The separation distance  $d_s$  improves from 0.796 m to 1.881 m, indicating enhanced safety margins and more reliable avoidance behavior. These results clearly demonstrate that the DR-CVaR trigger is essential for improving safety. Note that the success rate of ACBF can also be improved with DR-CVaR OFF by increasing both  $H_{\min}$  and  $H_{\max}$ , but at the cost of slower reaction time. Thus, the DR-CVaR trigger enables fast reaction.

## V. HARDWARE EXPERIMENTS

### A. Experimental Setup

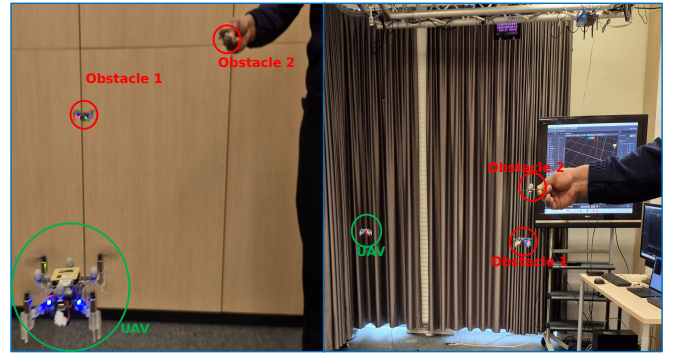


Fig. 3. Experimental lab setup. (Left) The green Crazyflie UAV must avoid two dynamic obstacles (marked in red): an approaching UAV and a thrown object. (Right) The motion-capturing system provides position data of the UAV and the obstacles. A video of our experiments is available for review.

The hardware experiments demonstrate the real-time performance of our DR-ACBF DOA and are based on a Bitcraze Crazyflie 2.1 UAV equipped with a flow deck sensor<sup>1</sup> and

<sup>1</sup><https://www.bitcraze.io/>

an onboard fly unit. Contrary to the simulation study with long flight distances, hardware experiments were limited by our OptiTrack motion capture perception area of about  $2\text{ m} \times 3\text{ m}$ . OptiTrack provides position data of the UAV and the obstacles at 120 Hz, which are tracked by the GNN-based SAFE-IMM obstacle tracker.

We have taken various Crazyflie limitations, including size, actuation bounds (acceleration, braking, and maneuvers), system latency, and clearance requirements, into consideration for our setup. We have adopted a similar metric for evaluation as used for our simulation study, and additionally measure the avoid time  $t_a$  and the detection time  $t_d$ . The avoid time is the duration from the start of the avoid action to the end of hovering. The detection time is the duration from the first detection of the obstacle until the avoidance command is issued.

We use a Linux-based, CPU-only laptop as the base station, which was configured to capture both the obstacles and the UAV from OptiTrack. The position data was integrated into MATLAB via a Python bridge on the base station. Communication between the base station and UAV was established via the Crazyflie MATLAB-Python API at 100 Hz using full-state setpoints (position, velocity, acceleration, and attitude). The hardware setup uses the same DR-ACBF configuration as for the simulation study (see Section IV-A), except for  $\|a_e\|_\infty \leq 0.8\text{ m/s}^2$ ,  $R_{\text{uav}} = 0.10\text{ m}$  and  $R_{\text{obs}} = 0.10\text{ m}$ . Furthermore,  $d_{cl}$  is set to  $0.05\text{ m}$  and  $t_{hd}$  to  $0.2\text{ s}$  with the braking configuration: time to stop  $t_s$  within  $0.7\text{ s}$  and braking intensity  $k_s = 0.2$ .

## B. Experimental Results

We conduct two hardware experiments. In the first experiment, the UAV hovers at a fixed position, avoids an obstacle thrown by a human, and returns to the hovering position. In the second experiment, the hovering UAV avoids a directly approaching UAV and a human-thrown object.

TABLE IV  
CRAZYFLIE AVOIDING ONE DYNAMIC OBSTACLE WITH DR-ACBF.

Flight	$v_{cl}$ (m/s)	$t_r$ (ms)	$t_{cm}$ (ms)	$t_a$ (ms)	$t_d$ (ms)	$d_s$ (m)
1	2.26	50.0	39.7	232	3866	0.205
2	2.56	66.5	61.5	283	3617	0.863
3	3.44	66.8	59.0	233	2999	0.393
4	3.66	66.9	60.7	233	3049	0.239
5	3.60	82.8	80.7	216	2516	0.695
6	2.96	66.1	53.2	249	2533	0.202
7	2.87	66.9	48.7	200	3616	0.241
8	3.04	66.4	64.8	200	3866	0.276
9	2.82	66.8	64.4	216	3683	0.337
10	3.11	66.4	59.1	250	3033	0.213
Mean	3.03	66.6	59.2	231	3277	0.366

Table IV presents the results of 10 flights of the first experiment using our DR-ACBF framework. In all flights, the UAV successfully avoided the thrown obstacle, which had a closing velocity  $v_{cl}$  between  $2.26\text{ m/s}$  and  $3.66\text{ m/s}$ . The time measurements demonstrate the responsiveness and

ability to execute avoidance actions efficiently. The reaction time  $t_r$  was less than  $67\text{ ms}$  in 9 flights, only in flight #5 it was measured as  $82.8\text{ ms}$ . Similarly, the average command time  $t_{cm}$  was  $59.18\text{ ms}$ , while the mean avoidance duration was  $0.231\text{ ms}$ . In all flights, the detection times  $t_d$  were above  $2.5\text{ s}$  with a mean of  $3.277\text{ s}$ , indicating a robust obstacle detection and tracking as well as an accurate response only when the obstacle is classified as unsafe. The separation distance  $d_s$  between the UAV and the obstacle was always larger than  $0.2\text{ m}$  with a mean of  $0.365\text{ m}$ , ensuring collision-free operation within the tested environment. Notably, flights #1 and #4 exhibited the safe separation distances ( $0.205\text{ m}$  and  $0.239\text{ m}$ , respectively), corresponding to the slowest and fastest velocities ( $2.26\text{ m/s}$  and  $3.66\text{ m/s}$ ).

TABLE V  
CRAZYFLIE AVOIDING TWO DYNAMIC OBSTACLES WITH DR-ACBF.

Obstacle	Flight	$v_{cl}$ (m/s)	$t_r$ (ms)	$t_{cm}$ (ms)	$t_a$ (ms)	$t_d$ (ms)	$d_s$ (m)
1	1	1.99	82.8	56.0	233	1884	0.201
	2	2.37	58.2	39.4	208	421	0.486
	3	2.86	59.1	34.7	184	342	0.281
	4	3.10	49.5	36.9	158	374	0.390
	5	1.43	58.1	40.5	116	375	0.267
	Mean	2.35	61.5	41.5	180	671	0.325
2	1	1.21	141.6	113.2	216	5050	0.657
	2	1.25	80.6	62.1	214	5167	0.780
	3	1.44	83.3	68.8	241	3766	0.550
	4	1.74	92.3	68.5	200	3732	0.738
	5	1.80	99.3	80.7	216	3517	0.702
	Mean	1.49	99.4	78.7	217	4246	0.685

Table V presents the results of the second experiment, where the UAV successfully avoided the two obstacles in all five flights. For the approaching UAV (obstacle 1), the average closing velocity  $v_{cl}$  was  $2.35\text{ m/s}$ . We measured similar reaction and command times as in the first experiment (mean values for  $t_r$  of  $61.54\text{ ms}$  and for  $t_{cm}$  of  $41.50\text{ ms}$ ). The avoidance duration was on average  $0.18\text{ s}$ , while the mean detection time  $t_d$  was  $0.67\text{ s}$ . The mean separation distance  $d_s$  was  $0.325\text{ m}$ , confirming safe maneuvering performance. For obstacle 2, which involved a more unpredictable human-thrown object, the average  $v_{cl}$  decreased to  $1.49\text{ m/s}$ . The mean reaction and command times  $t_r$  and  $t_{cm}$  increased to  $99.42\text{ ms}$  and  $78.66\text{ ms}$ , respectively, while the average avoidance duration  $t_a$  slightly increased to  $0.217\text{ s}$ . The mean detection time  $t_d$  significantly increased to  $4.25\text{ s}$ , indicating that the object was detected early and entered the avoidance trigger after some time. Despite these changes, the UAV maintained a safe separation  $d_s$  of  $0.685\text{ m}$  from obstacle 2.

Finally, an important finding of the hardware experiments was that the separation distance  $d_s$  was above the  $R_{\text{sum}}$  bound of  $0.200\text{ m}$ . DR-ACBF was able to satisfy the specified safety constraint for all flights.

## VI. CONCLUSIONS

In this paper, we presented a distributionally robust acceleration-level safety filter that enforces collision avoidance through linear, half-space constraints on the com-

manded acceleration. Our DR-ACBF attains real-time avoidance without solving QPs. Simulation studies against three baseline methods demonstrate that DR-ACBF achieves comparable success rates and safety margins, while reducing computation and command times, thereby improving responsiveness for fast DOA. The sensitivity analysis confirms robustness to key design parameters, with high success rates. An ablation study further demonstrates that the DR-CVaR trigger is crucial for risk-aware operation. Crazyflie experiments demonstrate that DR-ACBF achieves reliable DOA on resource-limited platforms bridging the gap between formal safety and practical real-time performance. Future work will extend this framework to integrate RADAR or vision sensing modality with a medium-sized UAV platform to assess the applicability of the proposed framework.

## REFERENCES

- [1] B. Rinner, C. Bettstetter, H. Hellwagner, and S. Weiss, "Multidrone systems: More than the sum of the parts," *Computer*, vol. 54, no. 5, pp. 34–43, 2021.
- [2] D. Falanga, S. Kim, and D. Scaramuzza, "How fast is too fast? the role of perception latency in high-speed sense and avoid," *IEEE Robotics and Automation Letters*, vol. 4, no. 2, pp. 1884–1891, 2019.
- [3] D. Mandaokar and B. Rinner, "Evaluating millimeter-wave radar for resource-efficient drone perception," in *Proc. International Conference on Distributed Computing in Smart Systems and the Internet of Things (DCOSS-IoT)*, 2025, pp. 352–359.
- [4] H. Chen, P. Lu, and C. Xiao, "Dynamic obstacle avoidance for uavs using a fast trajectory planning approach," in *Proc. IEEE International Conference on Robotics and Biomimetics (ROBIO)*, 2019, pp. 1459–1464.
- [5] C. S. Gadde, M. S. Gadde, N. Mohanty, and S. Sundaram, "Fast obstacle avoidance motion in small quadcopter operation in a cluttered environment," in *Proc. IEEE International Conference on Electronics, Computing and Communication Technologies (CONECCT)*, 2021, pp. 1–6.
- [6] Z. Xu and K. Shimada, "Quadcopter trajectory time minimization and robust collision avoidance via optimal time allocation," in *Proc. IEEE International Conference on Robotics and Automation (ICRA)*, 2024, pp. 16 531–16 537.
- [7] B. Lindqvist, S. S. Mansouri, A.-a. Agha-mohammadi, and G. Nikolakopoulos, "Nonlinear mpc for collision avoidance and control of uavs with dynamic obstacles," *IEEE Robotics and Automation Letters*, vol. 5, no. 4, pp. 6001–6008, 2020.
- [8] Z. Lin, L. Castano, E. Mortimer, and H. Xu, "Fast 3d collision avoidance algorithm for fixed wing uas," *Journal of Intelligent and Robotic Systems*, vol. 97, 2020.
- [9] A. Singletary, K. Klingebiel, J. Bourne, A. Browning, P. Tokumaru, and A. Ames, "Comparative analysis of control barrier functions and artificial potential fields for obstacle avoidance," in *Proc. IEEE/RSJ International Conference on Intelligent Robots and Systems (IROS)*, 2021, pp. 8129–8136.
- [10] W. Xiao, C. Belta, and C. G. Cassandras, "Adaptive control barrier functions," *IEEE Transactions on Automatic Control*, vol. 67, no. 5, pp. 2267–2281, 2022.
- [11] A. D. Ames, X. Xu, J. W. Grizzle, and P. Tabuada, "Control barrier function based quadratic programs for safety critical systems," *IEEE Transactions on Automatic Control*, vol. 62, no. 8, pp. 3861–3876, 2017.
- [12] A. D. Ames, J. W. Grizzle, and P. Tabuada, "Control barrier function based quadratic programs with application to adaptive cruise control," in *Proc. IEEE Conference on Decision and Control*, 2014, pp. 6271–6278.
- [13] J. Huang, J. Zeng, X. Chi, K. Sreenath, Z. Liu, and H. Su, "Dynamic collision avoidance using velocity obstacle-based control barrier functions," *IEEE Transactions on Control Systems Technology*, vol. 33, no. 5, pp. 1601–1615, 2025.
- [14] B. Dai, R. Khorrambakht, P. Krishnamurthy, V. Gonçalves, A. Tzes, and F. Khorrami, "Safe navigation and obstacle avoidance using differentiable optimization based control barrier functions," *IEEE Robotics and Automation Letters*, vol. 8, no. 9, pp. 5376–5383, 2023.
- [15] L. Marzari, F. Trotti, E. Marchesini, and A. Farinelli, "Designing control barrier function via probabilistic enumeration for safe reinforcement learning navigation," *IEEE Robotics and Automation Letters*, vol. 10, no. 10, pp. 9630–9637, 2025.
- [16] L. Knoedler, O. So, J. Yin, M. Black, Z. Serlin, P. Tsotras, J. Alonso-Mora, and C. Fan, "Safety on the fly: Constructing robust safety filters via policy control barrier functions at runtime," *IEEE Robotics and Automation Letters*, vol. 10, no. 10, pp. 10 058–10 065, 2025.
- [17] E. Daş and J. W. Burdick, "Robust control barrier functions using uncertainty estimation with application to mobile robots," *IEEE Transactions on Automatic Control*, vol. 70, no. 7, pp. 4766–4773, 2025.
- [18] T. G. Molnar, S. K. Kannan, J. Cunningham, K. Dunlap, K. L. Hobbs, and A. D. Ames, "Collision avoidance and geofencing for fixed-wing aircraft with control barrier functions," *IEEE Transactions on Control Systems Technology*, vol. 33, no. 5, pp. 1493–1508, 2025.
- [19] A. Alan, A. J. Taylor, C. R. He, A. D. Ames, and G. Orosz, "Control barrier functions and input-to-state safety with application to automated vehicles," *IEEE Transactions on Control Systems Technology*, vol. 31, no. 6, pp. 2744–2759, 2023.
- [20] Y. S. Quan, J. S. Kim, S.-H. Lee, and C. C. Chung, "Tube-based control barrier function with integral quadratic constraints for unknown input delay," *IEEE Control Systems Letters*, vol. 7, pp. 1730–1735, 2023.
- [21] H. Zhu, X. Zhu, and W. Yao, "Probabilistic multi-robot collision avoidance using chance-constrained safety barrier certificates," in *Proc. Chinese Control Conference (CCC)*, 2023, pp. 5817–5822.
- [22] K. Nguyen, S. Schoedel, A. Alavilli, B. Plancher, and Z. Manchester, "Tinympc: Model-predictive control on resource-constrained micro-controllers," in *Proc. IEEE International Conference on Robotics and Automation (ICRA)*, 2024, pp. 1–7.
- [23] J. A. Paulson, E. A. Buehler, R. D. Braatz, and A. Mesbah, "Stochastic model predictive control with joint chance constraints," *International Journal of Control*, vol. 93, no. 1, pp. 126–139, 2020.
- [24] A. Navsalkar and A. R. Hota, "Data-driven risk-sensitive model predictive control for safe navigation in multi-robot systems," in *Proc. IEEE International Conference on Robotics and Automation (ICRA)*, 2023, pp. 1442–1448.
- [25] S. Safaoui and T. H. Summers, "Distributionally robust cvar-based safety filtering for motion planning in uncertain environments," in *Proc. IEEE International Conference on Robotics and Automation (ICRA)*, 2024, pp. 103–109.
- [26] A. Chriat and C. Sun, "Wasserstein distributionally robust control barrier function using conditional value-at-risk with differentiable convex programming," in *Proc. AIAA SCITECH Forum*, 2024, p. 0725.
- [27] G. Olikier, A. Vuschmajew, and B. Vandereycken, "Gauss-southwell type descent methods for low-rank matrix optimization," *J. Optim. Theory Appl.*, vol. 206, no. 1, 2025.
- [28] H. Girgin, T. Löw, T. Xue, and S. Calinon, "Projection-based first-order constrained optimization solver for robotics," *ArXiv*, vol. abs/2306.17611, 2023. [Online]. Available: <https://api.semanticscholar.org/CorpusID:259309032>
- [29] D. Mandaokar and B. Rinner, "Safe-imm: Robust and lightweight radar-based object tracking on mobile platforms," 2025. [Online]. Available: <https://arxiv.org/abs/2511.20294>
- [30] J. Davila, L. Fridman, and A. Levant, "Second-order sliding-mode observer for mechanical systems," *IEEE Transactions on Automatic Control*, vol. 50, no. 11, pp. 1785–1789, 2005.
- [31] P. Sun, M. Li, Z. Yu, J. Li, R. Zhou, Y. Zhang, and Y. Cheng, "Robust adaptive fault-tolerant control of high-speed flight vehicle via high-order sliding-mode differentiator," in *Proc. International Conference on Industrial Artificial Intelligence (IAI)*, 2023, pp. 1–6.
- [32] G. Garimella, M. Sheckells, and M. Kobilarov, "Robust obstacle avoidance for aerial platforms using adaptive model predictive control," in *Proc. IEEE International Conference on Robotics and Automation (ICRA)*, 2017, pp. 5876–5882.
- [33] MathWorks, Inc., "Uav toolbox documentation." [Online]. Available: <https://de.mathworks.com/help/uav/index.html>
- [34] —, "Radardatagenerator: Generate radar detections in the form of pointcloud." [Online]. Available: <https://de.mathworks.com/help/radar/ref/radardatagenerator-system-object.html>